Estimation of Land Surface Temperature Over the Tibetan Plateau Based on Sentinel-3 SLSTR Data

Yuting Qi, Lei Zhong, Yaoming Ma, Yunfei Fu, Xian Wang, and Peizhen Li

***Abstract*—Land surface temperature (LST) plays a crucial role in the energy and water cycles of the Earth's climate system. The uncertainty of LST retrieval from satellites is a fundamental and long-standing issue, especially in plateau areas [such as the Tibetan Plateau (TP)], due to its high altitude, unique hydrometeorological conditions, and complex underlying surfaces. To improve the accuracy of LST retrieval over the TP, different methods, including the single channel (SC) algorithm, the split-window (SW) algorithm, and four machine learning (ML) models, were used to retrieve the LST based on sea and land surface temperature radiometer (SLSTR) data in this study. The validation results indicated that the root-mean-square errors (RMSEs) of the LSTs retrieved by the SC and SW algorithms were 3.48 and 2.64 K, respectively, which shows a better performance than the official SLSTR LST products (5.23 K). In addition, the random forest model has the highest accuracy among the four ML models, with an RMSE of 3.26 K. By comparing the performance of various methods, the SW algorithm is more stable and reliable for LST retrieval over the TP. In addition, the accurate spatiotemporal distribution of the LST based on the SW algorithm was also analyzed, which would benefit the understanding of the physical processes of energy and water cycles over the TP.**

***Index Terms*—Land surface temperature (LST), moderate resolution imaging spectroradiometer (MODIS)/terra, sea and land surface temperature radiometer (SLSTR) data, Tibetan Plateau (TP).**

I. Introduction

LAND surface temperature (LST) is a crucial parameter for water and energy flux exchange between the land surface and atmosphere [1], [2], [3]. It has been widely used to estimate evapotranspiration [4] and the urban heat island effect [5] and to monitor climate change [6]. The Tibetan Plateau (TP) has significant thermodynamic effects on atmospheric circulation, which is pivotal to climate change at different scales [7], [8], [9], [10]. Although many global and long-term LST products are available, LST uncertainty often exists on the TP due to its high altitude and heterogeneous underlying surface types compared with the plain area [11], [12].

LST can be obtained from ground observations, land surface modeling, and satellite remote sensing [13], [14]. The ground stations on the TP are not only sparse but also unevenly distributed due to heterogeneous surface conditions [10]. In the study of global-scale land-atmosphere interactions, it is difficult to use in situ measurements alone to meet the application requirements. In contrast, land surface modeling, such as the China land data assimilation system (CLDAS) [15], provides continuously spatiotemporal LSTs, but their spatial resolution is usually coarse. Satellite remote sensing has the characteristics of periodically and repeatedly observing the same area, which can provide long-term LST monitoring [16], [17]. According to the number of thermal infrared (TIR) bands involved, the two common LST retrieval methods based on remote sensing data are the single-channel (SC) and split-window (SW) methods [18], [19], [20], [21], [22]. The common advantages of these two algorithms are simplicity, high efficiency, and fewer prior assumptions, provided that the land surface emissivity (LSE) of each band is known. Currently, the SC method has been widely used for LST retrieval and is applicable to all TIR sensors [17], [21]. The core of using the SC algorithm to determine LST accurately is the selection of the radiative transfer equation (RTE), correctly considering the topographic effects and the complete atmospheric profile characteristics. Due to the unique hydrometeorological conditions and complex underlying surfaces of the TP, it is difficult to obtain synchronized atmospheric profile data. Compared with the traditional SC algorithm, the input parameters of the generalized SC algorithm are atmospheric water vapor content (WVC) and LSE, which are more convenient to obtain and more suitable for LST retrieval at a larger scale [18]. Meanwhile, the SW algorithm uses different parameterizations of crucial parameters without requiring accurate atmospheric profiles to retrieve the LST [19], [20]. The atmospheric transmittance will decrease at larger satellite zenith angle (SZA) because of the increased absorption path length. Error analysis demonstrates that the SW algorithm must fully take the SZA into account [13], [18]. In addition, in the humid atmosphere (WVC$>$2.5 g$\cdot$cm^{-2}),

Manuscript received 15 January 2023; revised 9 March 2023, 4 April 2023, and 13 April 2023; accepted 14 April 2023. Date of publication 19 April 2023; date of current version 8 May 2023. This work was supported in part by Second Tibetan Plateau Scientific Expedition and Research Program under Grant 2019QZKK0103, in part by the National Natural Science Foundation of China under Grant 41875031, Grant 42230610, Grant 41522501, and Grant 41275028, and in part by the CLIMATE-Pan-TPE in the Framework of the ESA-MOST Dragon 5 Programme under Grant 58516. *(Corresponding author: Lei Zhong.)*

Yuting Qi, Yunfei Fu, Xian Wang, and Peizhen Li are with the School of Earth and Space Sciences, University of Science and Technology of China, Hefei 230026, China (e-mail: qiyuting@mail.ustc.edu.cn; fyf@ustc.edu.cn; wang000@mail.ustc.edu.cn; lipz@mail.ustc.edu.cn).

Lei Zhong is with the School of Earth and Space Sciences, University of Science and Technology of China, Hefei 230026, China, and also with the CAS Center for Excellence in Comparative Planetology, Hefei 230026, China (e-mail: zhonglei@ustc.edu.cn).

Yaoming Ma is with the Land-Atmosphere Interaction and its Climatic Effects Group, State Key Laboratory of Tibetan Plateau Earth System, Resources and Environment, Institute of Tibetan Plateau Research, Chinese Academy of Sciences, Beijing 100101, China, and also with the College of Earth and Planetary Sciences, University of Chinese Academy of Sciences, Beijing 100049, China (e-mail: ymma@itpcas.ac.cn).

Digital Object Identifier 10.1109/JSTARS.2023.3268326

the WVC must be explicitly included in the SW algorithm [18]. The split-window algorithm (SWA) proposed by Becker and Li [13] explicitly incorporates the LSEs, SZA, and WVC, and it has been proven to with good performance over the TP [2]. In addition, Wan and Dozier [22] developed a generalized split-window (GSW) algorithm to retrieve LST from AVHRR and moderate resolution imaging spectroradiometer (MODIS) data, which also involved the LSEs, SZA, and WVC as input parameters. As one of the official algorithms for MODIS LST products, the GSW algorithm was utilized for LST retrieval under clear-sky conditions. Meanwhile, the thermal infrared band settings of the SLSTR sensor are similar to those of the MODIS sensor. Therefore, by fully considering the sensor characteristics and algorithm applicability, the SW algorithm proposed by Becker and Li [13] was selected to retrieve LST based on SLSTR data over the TP, and the MODIS LST products (MOD11A1) based on the GSW algorithm were used for comparison in this study. In practical applications, effective methods of LST retrieval from remote sensing data can be first obtained by taking into account the assumptions of algorithms, the characteristics of sensors, geographical characteristics, and atmospheric conditions of the study area. Then, the optimal method can be selected by comparing the performance of different algorithms. Unfortunately, comparisons are seldom made for different algorithms to retrieve LST on the TP [18].

In recent years, machine learning (ML) models have been widely developed and have played a significant role in research on environmental parameter retrieval [23], [24], [25], [26], [27]. ML models are suitable for establishing complex nonlinear statistical relations between satellite data and ground observations. Feasible ML models based on remote sensing data for LST retrieval can overcome some complex issues, such as limitations of observation instruments, cloud contamination, and atmospheric effects [17]. Wang et al. [23] proposed a novel LST retrieval method based on model-data-knowledge-driven and deep learning (DL). The validation with in situ measurements shows that the root-mean-square error (RMSE) obtained by the optimal band combination is approximately 1.22 K. Wang et al. [17] proposed a retrieval scheme using a random forest (RF) model suitable for different underlying surface conditions to retrieve LST on the TP. However, the uncertainty of using ML models is that they require multitudinous training data to build complex structures, have explanation problems for specific models, and do not consider the spatiotemporal correlation of environmental variables. Various problems lead to different results from different models when using the same inputs, so the performance of multiple models should be compared with each other. The application of LST retrieval based on the ML model still needs further exploration, and three ML models and one DL model are utilized in this study to retrieve LST on the TP.

The sea and land surface temperature radiometer (SLSTR) sensor carried by Sentinel satellites was launched in 2016 with three thermal infrared bands, which provided new data sources for LST retrieval and delivered geophysical Level-2 LST products [28], [29]. The SW algorithm was used to produce SLSTR LST products, in which the base retrieval coefficients are determined by regressing the simulated brightness temperatures (BTs) with the known in situ measurements [19]. Several regional LST retrieval methods based on the SW algorithms have been proposed since the first SLSTR image acquisition [19], [20]. Yang et al. [19] compared seventeen widely explicitly LSE-dependent SW algorithms based on SLSTR data. Validation results confirmed that two SW algorithms have high accuracy with RMSE ranges of 0.49 to 0.61 K in Lake Constance. Zheng et al. [20] developed an SW algorithm to estimate LST based on SLSTR data, in which the algorithm coefficients were optimized by division into tractable subranges according to the view zenith angle, column water vapor, and BT. Meanwhile, a new physical SC algorithm was proposed to retrieve LST from Landsat-8 TIRS Band 10 and successfully evaluated with simulated and in situ data [21]. However, the study areas focused by previous studies are relatively flat terrain. Due to the high altitude, unique hydrometeorological conditions, and complex underlying surfaces over the TP, LST uncertainty usually exists in different retrieval algorithms over the TP. In addition, the available observation stations on the plateau are not only sparse but also unevenly distributed, which leads to few studies assessing the applicability of Sentinel-3 Level-2 SLSTR LST products over the TP. This study first evaluated the performance of SLSTR LST products on the TP and then used three different methods to retrieve LST based on SLSTR data. The purposes of this study mainly include two aspects. By comparing the performance of various algorithms, an improved LST retrieval method suitable for TP was developed based on SLSTR data. Furthermore, a high-accuracy LST spatiotemporal distribution over the entire TP was obtained, which would benefit the understanding of the physical processes of energy and water cycles over the TP.

This study aims to 1) improve the LST retrieval accuracy from Sentinel-3 SLSTR data over the TP by comparing the performance of different methods and 2) obtain an optimized spatiotemporal distribution over the TP. In this study, two general algorithms and four ML models were used for LST retrieval from Sentinel-3 SLSTR LST data over the TP. The study area and data used in this article are shown in Section II. Section III shows the methodology used in this study. The retrieved LST results and their spatiotemporal distribution over the TP are highlighted in Section IV. The discussion is described in Section V. Finally, Section VI concludes this article.

II. Study Area and Data

A. Study Area

The TP has long been recognized as one of the crucial regions for climate change at different spatiotemporal scales (see Fig. 1) [30], [31]. The TP exerts strong thermal forcing on the atmosphere over the Asian monsoon region, and its environmental changes are mostly associated with rapid surface warming. It is essential to accurately monitor the spatiotemporal distribution of the LST over the TP based on different satellite sensors.

B. Data

1) Remote Sensing Data: Sentinel-3 was launched on February 16, 2016 and carried a sea and land surface temperature

TABLE I
BAND INFORMATION AND ITS APPLICATIONS OF EACH CHANNEL OF SENTINEL-3 SLSTR

Band name	Central wavelength	Band width	Spatial resolution	Function
Green:S1	0.554 μm	0.019 μm	0.5 km	Chlorophyll, dual-view AOD over land
Red:S2	0.659 μm	0.019 μm	0.5 km	Vegetation Index, dual-view AOD over land
NIR:S3	0.868 μm	0.020 μm	0.5 km	Vegetation Index, dual-view AOD over land
SWIR:S4	1.375 μm	0.021 μm	0.5 km	Thin Cirrus Cloud Detection
SWIR:S5	1.613 μm	0.061 μm	0.5 km	Clouds, Active Fire (at night as alternative to S6)
SWIR:S6	2.256 μm	0.050 μm	0.5 km	Clouds, Active Fire (at night)
TIR:S7	3.742 μm	0.398 μm	1.0 km	Night-time dual-view SST, Active Fire
TIR:S8	10.854 μm	0.776 μm	1.0 km	Dual-view SST/LST, Active Fire
TIR:S9	12.022 μm	0.905 μm	1.0 km	Dual-view SST/LST
F1	3.742 μm	0.398 μm	1.0 km	Active Fire
F2	10.854 μm	0.776 μm	1.0 km	Active Fire

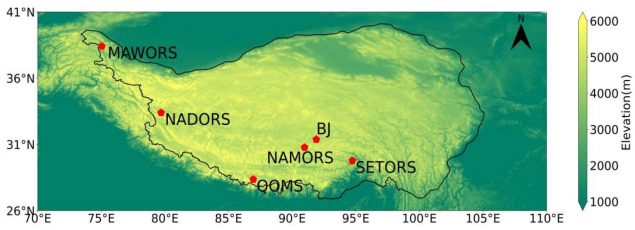

Fig. 1. Locations of the six comprehensive observation stations on the TP. The legend of the color map indicates the elevation.

radiometer (SLSTR) [32], [33]. SLSTR is a scanning radiometer with three thermal infrared bands (see Table I), which is designed to capture global land surface and sea surface temperatures. The SLSTR data utilized in this study are from the Copernicus Open Access Hub[1], including Level-1 radiation and Level-2 LST data. Level-1 data provided radiometric measurements that were geographically corrected for each SLSTR channel. In the Level-2 stage, an SWA is applied to process the S8 and S9 band data, and LST products are finally delivered [33]. Level-2 data also delivered auxiliary information for LST retrievals, such as fractional vegetation cover, land cover type, total column water vapor, SZA, and quality control flags. In addition, the Landsat images with a high spatial resolution of 30 m were used to evaluate the spatial representativeness of in situ measurements. The MODIS/Terra LST products (MOD11A1) and MODIS Level 1B Calibrated Radiances were used for comparison. The MODIS LST products were widely used for various studies, and their accuracy was evaluated based on different methods [34], [35]. Under clear-sky conditions, the RMSE of the C6 MODIS LST product is less than 2 K, and several studies demonstrated that there are some underestimations for MODIS nighttime LST product [34], [35]. The preprocessing of the remote sensing data involved three main steps:

a) quality control;
b) spatial collocation;
c) temporal concurrence.

However, there may be some differences between the SLSTR and MODIS due to different sensor parameters and operating orbit settings. The Sentinel-3 A&B approximate observation times are 2:00–6:00 (UTC) in the ascending orbit and 13:00–17:00 (UTC) in the descending orbit over the TP. The approximate observation times of the MOD11A1 products are 3:00–7:00 (UTC) in the ascending orbit and 13:00–17:00 (UTC) in the descending orbit over the TP.

2) *Reanalysis Data and in Situ Measurements:* In this study, CLDAS V2.0 was used to calculate the atmospheric total column water vapor (TCWV), which is one of the critical parameters for LST retrieval. CLDAS V2.0 has high accuracy, with 1 h temporal resolution and 0.0625° spatial resolution, covering the entire East Asian region [15]. The kriging interpolation method was used to downscale the data to a 1 km resolution. Three meteorological parameters of CLDAS V2.0 are obtained, including the near-surface air temperature T_a, specific humidity q (both measured at 2 m), and air pressure p [15].

The Tibetan Observation and Research Platform (TORP) aims to research the land-atmosphere interaction over the TP and consists of six comprehensive observations (see Table II): SETORS, BJ, QOMS, NADORS, NAMORS, and MAWORS [10]. The MAWORS station is situated in the northwestern TP, surrounded by large-scale glaciers, whose land type is predominantly sandy soil. The NADORS station is located in an open valley covered by desert and gravel. The BJ station was built in a flat prairie

[1](https://scihub.copernicus.eu)

TABLE II
DETAILS OF THE MEASUREMENTS AT SIX STATIONS

Stations	Latitude	Longitude	Elevation	Land cover	Soil type	Land cover within 1 km around the station
BJ	31.37° N	91.90° E	4509 m	Alpine meadow	Sandy silt loam	Grassland
QOMS	28.36° N	86.95° E	4298 m	Alpine desert	Sand and gravel	Grassland and bareland
MAWORS	38.41° N	75.05° E	3668 m	Alpine desert	Sand and gravel	Grassland
NAMORS	30.77° N	90.98° E	4730 m	Alpine steppe	Sandy silt loam	Grassland
SETORS	29.77° N	94.73° E	3327 m	Alpine meadow	Sandy clay loam	Grassland and forest
NADORS	33.39° N	79.70° E	4270 m	Alpine desert	Sand and gravel	Bareland

with high grass density, whose soil type is predominantly silt loam. The NAMORS station is situated near Nam Co Lake and is covered with alpine meadows. The QOMS station lies in the Rongbuk Valley, and the land cover type is grassland. The SETORS station is located in the southeastern TP and close to the mountain valley, where the dominant land type is alpine meadow. The in situ longwave radiation data from six stations were obtained to calculate the in situ LST, and the linear interpolation method was used to match the satellite transit times [10]. The upward and downward longwave radiation fluxes were measured by CNR1 net radiometer from Kipp and Zonen equipped at TORP stations. The FOV of the CNR1 is 150°. The four-component radiation flux system CNR1 was installed at the height of 1.5 m, and the diameter of its detection circular at the surface is approximately 12 m [10]. In addition, the SC algorithm was used to obtain LST on clear days based on Landsat images with a spatial resolution of 30 m to assess the spatial representativeness of ground-based LST. The uncertainty of LST within 1 km of the station area should be less than 1 K to meet the requirements of homogeneity validation [3].

The in situ LST was retrieved from longwave radiation data from six stations based on the Stefan–Boltzmann law [1], [2]

$$T_S = \left(\frac{\mathrm{LWU} - (1 - \varepsilon_b)\,\mathrm{LWD}}{\sigma \varepsilon_b} \right)^{\frac{1}{4}} \tag{1}$$

where T_S is the in situ LST; LWU and LWD are the surface upwelling longwave radiation and atmospheric downwelling longwave radiation obtained from TORP, respectively; ε_{b} is the land surface broadband emissivity; and σ expresses the Stefan–Boltzmann constant ($5.67\times10-8$ W·m^{-2}·K^{-4}).

The practical retrieval algorithm of LSE is mainly semiempirical methods based on remote sensing, including the normalized difference vegetation index (NDVI)-based emissivity (NBE) and classification-based emissivity methods [36], [37], [38]. The NBE method can distinguish different land cover types, such as bare soil, vegetation, and their mixture. Meanwhile, the surface pixels of the TP are heterogeneous within 1 km spatial resolution. Therefore, an improved NBE method is used by comprehensively considering the surface characteristics of the TP and SLSTR sensor parameters. Specifically, the key is to calculate the additional item for coarse and heterogeneous pixels, which depends on the surface characteristics and considers the cavity effect. Since it cannot be estimated from the remote sensing spectrum, it is usually assumed that the average value of different surface geometric distributions is 0.015. In addition, the NDVI$^{\mathrm{THM}}$ algorithm of Sobrino et al. [39] was also used to retrieve LSE for comparison and finally the algorithm was selected currently. Here, the LSE was estimated from the SLSTR by the using following equations [36], [38]:

$$\varepsilon_b = \varepsilon_v\, P_v + \varepsilon_s\,(1 - P_v) + 4\,\langle d\varepsilon \rangle\, P_v\,(1 - P_v) \tag{2}$$

where ε_v= 0.98 represents the full vegetation emissivity and ε_s= 0.96 represents the bare soil emissivity; $\langle d\varepsilon \rangle$ is the cavity effect of rough surfaces, set to 0.015; and P_v is the proportion of vegetation calculated via

$$P_v = \frac{\mathrm{NDVI} - \mathrm{NDVI_{min}}}{\mathrm{NDVI_{max}} - \mathrm{NDVI_{min}}} \tag{3}$$

where the normalized difference vegetation index (NDVI) was estimated from

$$\mathrm{NDVI} = \frac{\rho 3 - \rho 2}{\rho 3 + \rho 2} \tag{4}$$

where $\rho 2$ and $\rho 3$ are the narrowband reflectances of band 2 and band 3 of SLSTR, respectively, and $\mathrm{NDVI_{min}}$ and $\mathrm{NDVI_{max}}$ are NDVI values for bare soil and full vegetation, respectively. According to the actual situation in the TP, $\mathrm{NDVI_{min}}$ is set to 0, and $\mathrm{NDVI_{max}}$ is set to 0.8 [2].

III. METHODOLOGY

A. SC Algorithm

The SC algorithm is convenient for sensors, such as ETM+ with only one thermal infrared band [21]. Combining the sensor band setting, atmospheric absorption characteristics, and radiation peak wavelength corresponding to the average LST on the TP, the S8 band of the SLSTR was selected for LST retrieval. The detailed process of using the SC algorithm to retrieve LST from the SLSTR Level-1 data is shown in Fig. 2(a). The accuracy of the generalized SC algorithm for retrieving LST depends on the selection of the RTE, the accuracy of LSE, and the atmospheric transmittance data [18]. The main formula of the SC algorithm

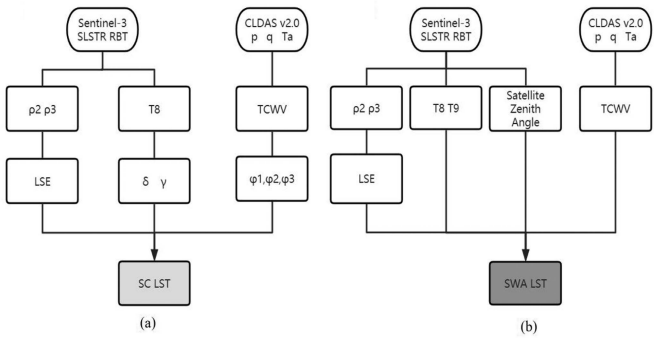

Fig. 2. Flowchart for retrieving LST from sentinel-3 SLSTR data. (a) Retrieval process of the SC algorithm. (b) Retrieval process of the SW algorithm.

is expressed as follows [17]:

$$\mathrm{LST_{SC}} = \gamma\left[\frac{\varphi 1 Ls + \varphi 2}{\varepsilon_b} + \varphi 3\right] + \delta \tag{5}$$

where $\mathrm{LST_{SC}}$ is the SC-based LST and ε_b is the LSE obtained from (2)–(4); $\varphi 1$, $\varphi 2$, and $\varphi 3$ are the atmospheric functions (AFs), which are composed of three parameters and calculated by the atmospheric WVC (ω); Ls is the radiation (in $\mathrm{W{\cdot}m^{-2}{\cdot}sr^{-1}{\cdot}mm^{-1}}$) from the SLSTR S8 band, which can be obtained by integrating the Planck function of BT in each band; γ and δ are two indirect parameters related to Planck's function, which can be determined by the following formulae:

$$\gamma = \frac{C_2 Ls}{T_b^2}\left[\frac{\lambda^4 Ls}{C_1} + \lambda^{-1}\right]^{-1} \tag{6}$$

$$\delta = -\gamma Ls + T_b \tag{7}$$

where C_1 and C_2 are Planck's constants ($C_1 = 1.19104 \times 108\ \mathrm{W{\cdot}mm^4{\cdot}m^{-2}{\cdot}sr^{-1}}$, $C_2 = 1.43877 \times 10^4$ mm·K); λ is the central wavelength of the SLSTR sensor S8 band, which equals 10.85 μm; and Tb is the BT of the SLSTR S8 band (K).

The $\varphi 1$, $\varphi 2$, and $\varphi 3$ in (5) are three parameters in AFs, which are determined by the atmospheric WVC (ω)

$$\begin{pmatrix}\varphi 1\\ \varphi 2\\ \varphi 3\end{pmatrix} = \begin{pmatrix}k_{11} & k_{12} & k_{13}\\ k_{21} & k_{22} & k_{23}\\ k_{31} & k_{32} & k_{33}\end{pmatrix}\begin{pmatrix}\omega^2\\ \omega\\ 1\end{pmatrix} \tag{8}$$

where k_{11}– k_{33} are the coefficients for AFs; ω is the atmospheric water vapor content (WVC), which can be calculated based on three meteorological data from CLDAS using the following equation [40], [41], [42]:

$$\omega = 0.00493\frac{\mathrm{RH}}{T_\mathrm{a}}\exp\left(2623 - \frac{5416}{T_\mathrm{a}}\right) \tag{9}$$

where ω is the atmospheric total column water vapor (TCWV, in units of $\mathrm{g{\cdot}cm^{-2}}$), T_a is the air temperature (K), and RH is the relative humidity (%), which can be calculated via

$$\mathrm{RH} = 100\frac{V_a}{V_s} \tag{10}$$

TABLE III
COEFFICIENTS OF AFS FOR CLDAS DATA USED IN THE SC ALGORITHM

Database	k_{ij} (i=1,2,3; j=1,2,3)		
CLDAS	-1.3282	3.6352	-1.9225
	2.9753	-4.3239	6.7123
	2.9337	-4.2634	6.6183

in which $\mathrm{V_a}$(Pa) and $\mathrm{V_s}$(Pa) are the actual and saturated water vapor pressures, respectively

$$V_a = \frac{P}{0.378 + \frac{0.622}{q}} \tag{11}$$

$$V_s = 611.2\exp\left(17.67\frac{T_a - 273.15}{T_a - 29.65}\right) \tag{12}$$

where p is the air pressure (Pa) and q is the specific humidity ($\mathrm{kg{\cdot}kg^{-1}}$) [4].

The coefficients k_{ij} used to calculate AFs vary for different datasets and can be obtained by simulations. However, synchronized atmospheric profile data over the TP cannot be obtained, and the limited radiosonde data cannot represent the entire TP because of its unique characteristics. Therefore, the radiative transfer mode such as MODTRAN was not used to simulate the coefficients. Instead, the AFs were entered into (5) to express the quadratic relationship, and these coefficients were fitted to the in situ measurements by linear regression (LR). Totally 2933 in situ LST samples were used to train the LR model. New coefficients (k_{ij}) with higher accuracy were proposed (see Table III).

B. SW Algorithm

There are currently two main SW algorithms that fully take the LSEs, WVC, and SZA into consideration [18]. The MOD11A1 LST products retrieved by the GSW algorithm under clear-sky conditions were used for comparison in this study. The SW algorithm proposed by Becker and Li [13] has been proven to have good accuracy over the TP, and it will be used as the retrieval algorithm in this study [2]. For the SW algorithm, the coefficients need to be determined in advance either by simulating the satellite signals with atmospheric and surface parameters based on radiative transfer model or by empirically building relationship between the satellite signals and in situ LST measurements [18]. Although the former method has solid physical basis, the synchronized atmospheric profile data were extremely difficult to obtain. Therefore, the LSEs, WVC, and SZA were comprehensively considered in the LST retrieval algorithm, and the coefficients were obtained via multiple LR model [2], [13].

The process of using the SW algorithm to retrieve LST from SLSTR data is shown in Fig. 2(b). In this study, the LST was retrieved using thermal infrared bands (S8 and S9) combined with SZA data, and the LSE calculated by (2)–(4). The main

formula can be expressed as [13]

$$\begin{aligned}\mathrm{LST}_{\mathrm{SWA}} = a_0 \; &+ a_1\omega + [a_2 + (a_3 + a_4\omega\cos\theta) \\ &\times (1-\bar{\varepsilon}) - (a_5 + a_6\omega)\,\Delta\varepsilon]\,\frac{T_8+T_9}{2} \\ &+ [a_7 + a_8\omega + (a_9 + k_{10}\omega) \\ &- (a_{11} + a_{12}\omega)\,\Delta\varepsilon]\,\frac{T_8-T_9}{2} \end{aligned} \tag{13}$$

where $\mathrm{LST}_{\mathrm{SWA}}$ is the LST retrieval based on the SW algorithm (K); T_8 and T_9 are the BTs (K) of Sentinel-3 SLSTR band 8 and band 9, respectively; and ω is the water vapor content (WVC, g·cm^{-2}), which was obtained via (9)–(12); θ is the SLSTR view zenith angle; a_0–a_{12} are the linear coefficients for LST retrieval, which can be obtained by LR; and $\bar{\varepsilon}$ and $\Delta\varepsilon$ are the average and the difference between the narrowband emissivities of band 8 (ε_8) and band 9 (ε_9) of Sentinel-3 SLSTR, respectively. $\bar{\varepsilon}$ and $\Delta\varepsilon$ can be obtained through the following expression [42]:

$$\bar{\varepsilon} = \frac{\varepsilon 8 + \varepsilon 9}{2} = 0.971 + 0.018 P_V \tag{14}$$

$$\Delta\varepsilon = \varepsilon 8 - \varepsilon 9 = 0.006\,(1 - P_V)\,. \tag{15}$$

C. Machine Learning Model

Although physical models can accurately and effectively establish the relationship between satellite observations and surface parameters, these methods tend to require many prior parameters. Such knowledge often has considerable uncertainty and leads to the limited accuracy of environmental parameter retrieval because of the high complexity of physical processes [23]. ML has powerful simulation capability, which can simplify physical models and establish nonlinear relationships for environmental parameter retrieval. The LR model is one of the ML models widely used in practice. It uses a linear function of input characteristics for prediction [23]. Since the training and prediction speed of the LR model is very fast, this model can be extended to large datasets and is also effective for sparse data. The decision tree (DT) model is widely used in classification and regression tasks. The DT model has two advantages: the obtained model is easy to visualize, and the algorithm is completely independent of data scaling. However, a significant disadvantage of the DT model is its overfitting problem. The RF model is a nonlinear ensemble ML model that is essentially a collection of multiple DTs. Each DT in the RF model is slightly different from the others, and the average value is taken to reduce the problem caused by overfitting [43]. BPNN is an essential neural network (NN) characterized by at least one hidden layer containing multiple nodes or neurons at the input and output layers [44]. The BPNN algorithm mainly includes forward and backward propagation, and the neurons in the input layer pass through each hidden layer by forward propagation. If the desired result is not obtained, through back propagation of errors, the weights of neurons in each hidden layer are updated iteratively to minimize them [44].

In this study, three ML models and a DL model were used to retrieve LST over the TP, and the input variables were shown in Table IV. The in situ LSTs were regarded as true values for training. Totally 4190 in situ LST samples from TORP were selected and divided into two parts: the training set consisted of 2933 samples, which accounted for 70% of the total dataset; the validation set consisted of 1257 samples, which accounted for 30% of the total dataset. The default settings in scikit-learn were selected for three ML models. For the BPNN model, the necessary parameter settings were the appropriate hidden layer and the number of neurons. Specifically, the number of hidden layers is set to 4, the number of neurons is set to 6, and the number of all hidden layers is the same. Except for the WVC, all other input data were from satellite data.

TABLE IV
INPUT VARIABLES FOR ML MODELS

Variables	Description	Datasets
ω	Total column water vapor content	CLDAS
B8	S8 band brightness temperature	SLSTR
B9	S9 band brightness temperature	SLSTR
ε	Land surface emissivity	SLSTR
H	Elevation	SLSTR
θ	Satellite zenith angle	SLSTR

D. Statistical Indices for Ground Validation

To evaluate the LST retrieval results obtained from different algorithms, four statistical indices, including RMSE, mean absolute error (MAE), mean bias (MB), R (Pearson correlation coefficient), and standard deviation (STD), were used in this study

$$\mathrm{RMSE} = \sqrt{\frac{\sum_{i=1}^{N}(y_i - x_i)^2}{N}} \tag{16}$$

$$\mathrm{MB} = \frac{\sum_{i=1}^{N}(y_i - x_i)}{N} \tag{17}$$

$$\mathrm{MAE} = \frac{\sum_{i=1}^{N}|y_i - x_i|}{N} \tag{18}$$

$$R = \frac{\sum_{i=1}^{N}[(x_i - \bar{x})(y_i - \bar{y})]}{\sqrt{\sum_{i=1}^{N}\left[(x_i - \bar{x})^2\right]}\sqrt{\sum_{i=1}^{N}\left[(y_i - \bar{y})^2\right]}} \tag{19}$$

$$\mathrm{STD} = \sqrt{\frac{\sum_{i=1}^{N}(y_i - \bar{x})^2}{N}}. \tag{20}$$

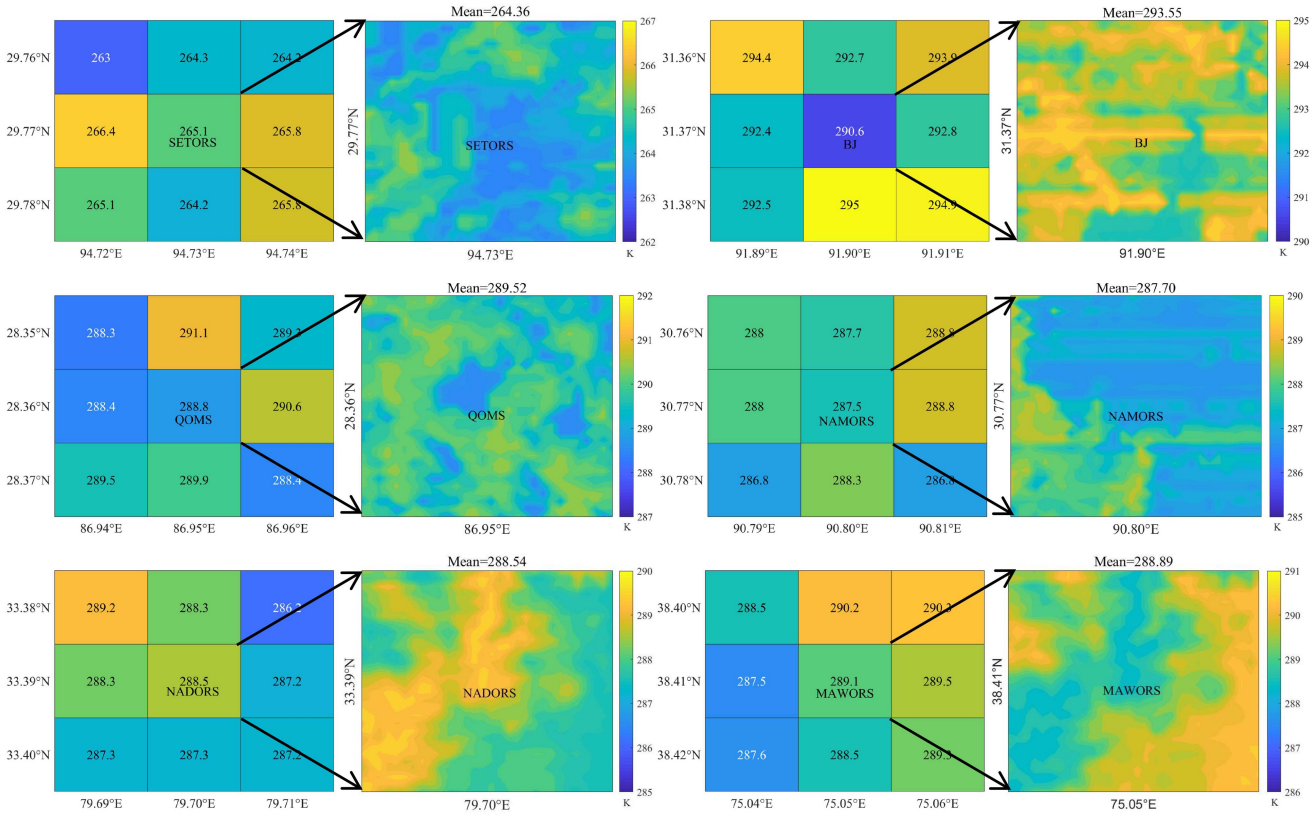

Fig. 3. Differences in the landsat LST images with subsets of 30×30 pixels within an SLSTR pixel at six stations. The left panels are the SLSTR Level-2 LST products, with a spatial resolution of 1 km. The right panels are Landsat SC-based LST, with a spatial resolution of 30 m.

IV. Results

A. Validation of LST Retrieval Algorithms

It is urgent to evaluate the performance of the retrieval algorithm independently because LST retrieval based on satellite data involves simplifications and correction processes. The main limitation of ground-based validation is that the in situ LST is not representative at the satellite pixel scale, especially for heterogeneous underlying surfaces (e.g., TP). Therefore, the SC algorithm was utilized to retrieve LST based on Landsat images with a high spatial resolution of 30 m around six research stations to evaluate the spatial representativeness of in situ measurements. The differences in the spatial distribution of the Landsat LST images with subsets of 30×30 pixels within an SLSTR pixel around six stations are shown in Fig. 3. The error between 30 m and 1 km satellite pixels at the six stations was calculated, and a total of 605 images were used for validation. At the satellite pixel scale, the results show that there is spatial heterogeneity of LST around the six stations. However, the results indicate that the mean STD of LST was less than 1 K, which means that the six stations were qualified for homogeneity validation [45] (see Table V).

Two years (2019–2020) of in situ measurements from six stations were processed to validate the retrieved LST results based on the SC and SW algorithms. In addition, MODIS and SLSTR LST products were used as complementary strategies for comparing algorithm performance. Both of these products

TABLE V
Statistical Indices of the Landsat LST Images With Subsets of 30×30 Pixels Within a Sentinel-3 SLSTR Pixel at Six Stations

Site name	STD (K)	N
BJ	0.92	102
QOMS	0.84	113
MAWORS	0.78	98
NAMORS	0.92	105
SETORS	1.14	88
NADORS	0.89	99
Mean	0.94	Total:605

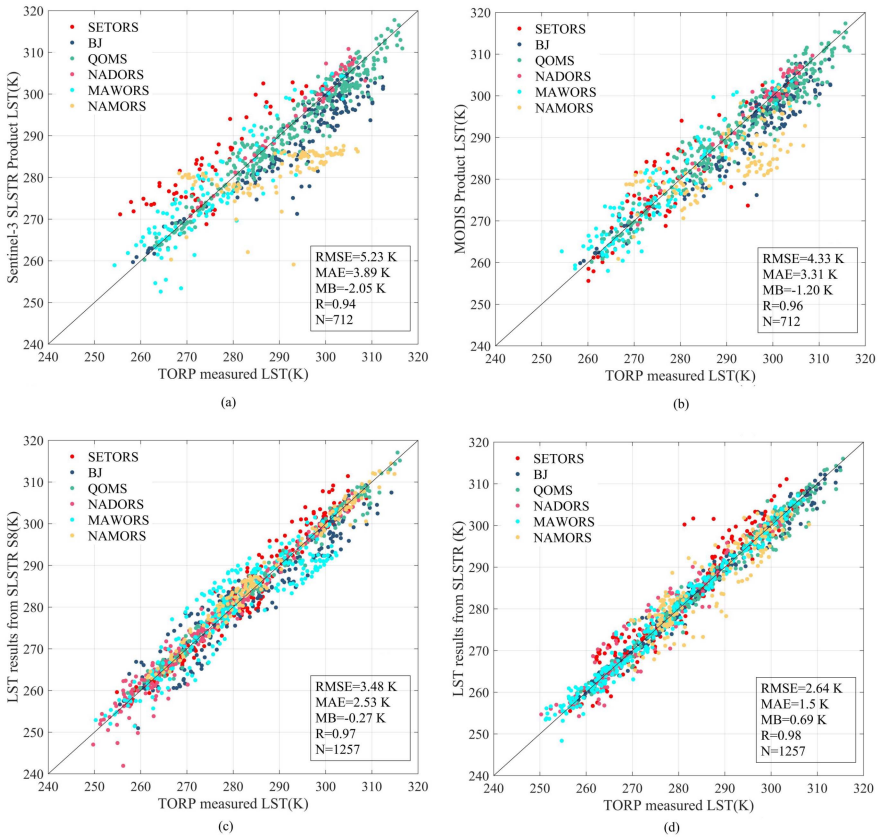

Fig. 4. Validation of the LST retrieved from Sentinel-3 SLSTR and MODIS data. (a) Sentinel-3 level-2 SLSTR LST products. (b) MODIS LST products. (c) SC method results from Sentinel-3 SLSTR. (d) SW method results from Sentinel-3 SLST.

use the SW algorithm to retrieve LST, and the spatial resolution is 1 km. As indicated in Fig. 4(a) and (b), the results show that the RMSE of the MODIS LST product (4.33 K) is less than that of the Sentinel-3 SLSTR LST product (5.23 K), and both have some underestimation to a certain extent. Especially at the NAMORS station, the LST was underestimated in SLSTR products when the LST was greater than 280 K, and similar results can be found in MODIS LST products. In contrast, the LST at SETORS stations was overestimated to a certain extent in SLSTR products. The performance of MODIS and Sentinel LST products in plateau areas needs to be improved. Therefore, the SC and SW algorithms and four ML models were utilized to retrieve LST over the TP based on Sentinel SLSTR data. Fig. 4(c) shows that the RMSE, MAE, MB, and R of LST retrieval from the SC algorithm were 3.48, 2.53, −0.27 (K), and 0.97, respectively. Moreover, Fig. 4(d) indicates that the RMSE, MAE, MB, and R of LST retrieval based on the SW algorithm were 2.64, 1.50, 0.69 (K), and 0.98, respectively. The performance of LST retrieved based on SC and SW algorithms was superior to SLSTR Level-2 LST products, which further indicates that the uncertainty of LST usually exists in different remote sensing land products. Compared with the SC algorithm, the SW algorithm with a smaller RMSE is more suitable for the TP. Research shows that to obtain the expected LST accuracy in wide regions, the SZA must also be taken into account, particularly for warm and humid atmospheres [3]. Different from the SC algorithm, the SW algorithm used in this study introduces the cosine of the SZA and utilizes the differential atmospheric absorption, which may result in the better performance of the SW algorithm.

In this study, three ML models and one DL model were used to retrieve the LST based on SLSTR data. The typical characteristic of the ML model is that it has extremely complex and deep structures, so a multitude of training data was required to build models. Since the Sentinel satellite was launched in 2016, the number of samples available for training has been quite limited. As a result, the accuracy of three ML models and one DL model is lower than that of the SW algorithm. As indicated in Fig. 5(a), the RMSE of the LR model is 4.35 K, which is the lowest accuracy among the four ML models. Moreover, Fig. 5(b)–(c) shows that the RMSE of the DT model is 3.91 K, and the RMSE of the RF model is 3.26 K. Traditional ML models such as RF, DT, and LR have a good performance, and it can be identified that the RF model has the highest accuracy in the case of limited training datasets. In addition, it can be expected that the effect of the ML model will be better with more training data. In recent years, DL models (such as the BPNN model) were developed from the traditional NN, which uses the most advanced state-of-the-art ML framework. The performance of the DL model is greatly improved and is superior to that of traditional models. However, the DL model is more suitable for big data, which leads to results that do not meet expectations

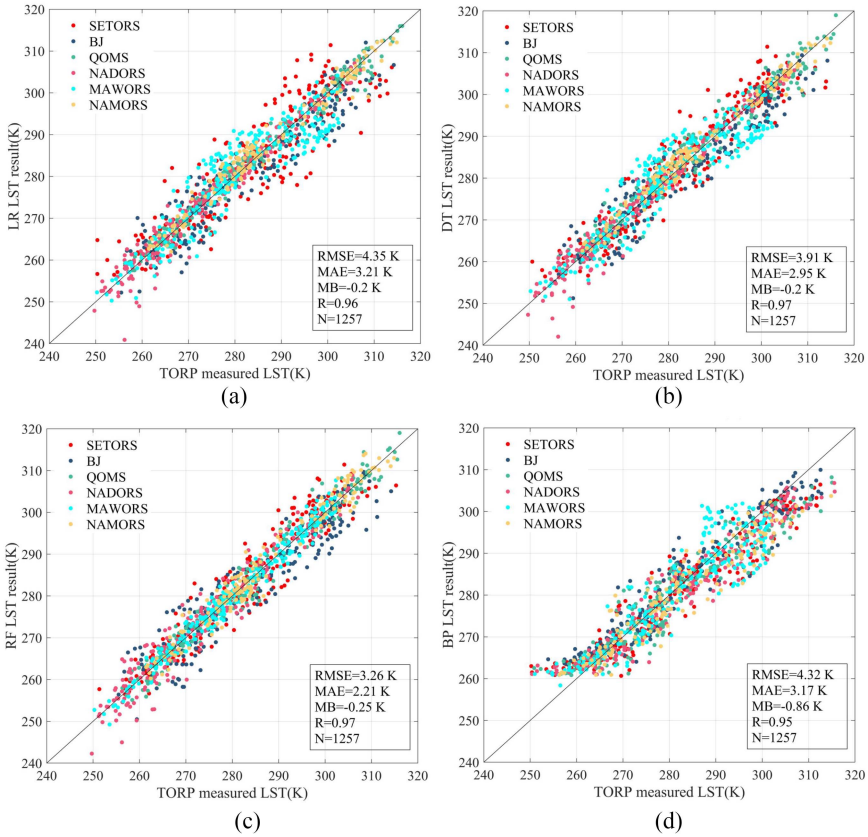

Fig. 5. Scatter plots between the retrieved LST results and in situ measurements. The retrieved LSTs were obtained from four ML models. (a) LR model. (b) DT model. (c) RF model. (d) BPNN model.

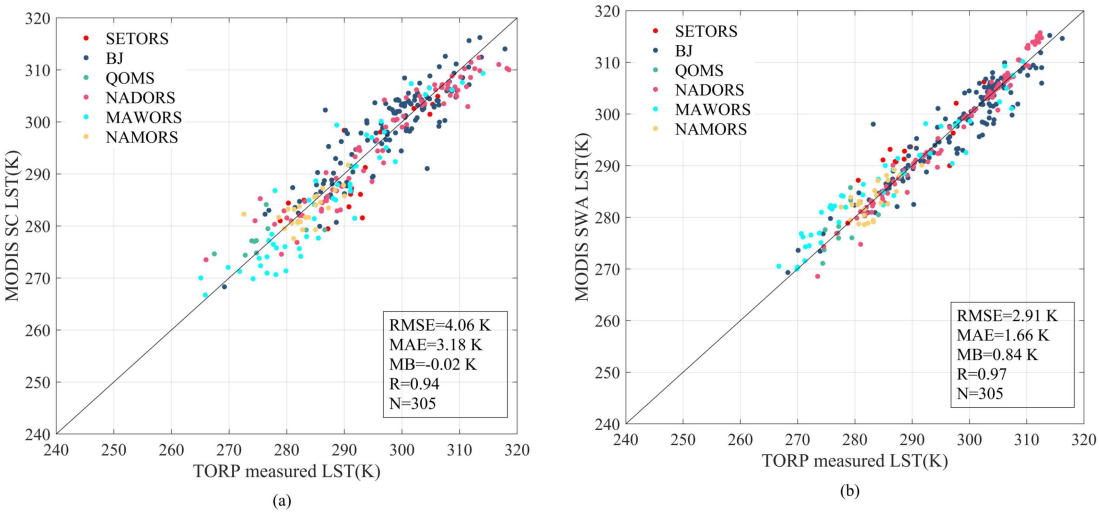

Fig. 6. Comparisons of the retrieved MODIS LST results against in situ measurements based on (a) SC method and (b) SW method.

due to limited input data. As shown in Fig. 5(d), the RMSE of the BPNN model is 4.32 K. In general, the application of the ML models in LST retrieval has a good performance, and the RF model is the best by comparison.

To validate the portability of the developed algorithms in this study, the improved SC and SW algorithms were used to retrieve LST from MODIS data over the TP. Fig. 6 shows that all the MODIS LST retrieval results have good agreement with in situ LST measurements, with RMSEs ranging from 2.91 K to 4.06 K and R ranging from 0.94 to 0.97. The MODIS LST retrieval results, however, show slightly degraded accuracy compared to the SLSTR LST retrieval results (with RMSEs ranging from

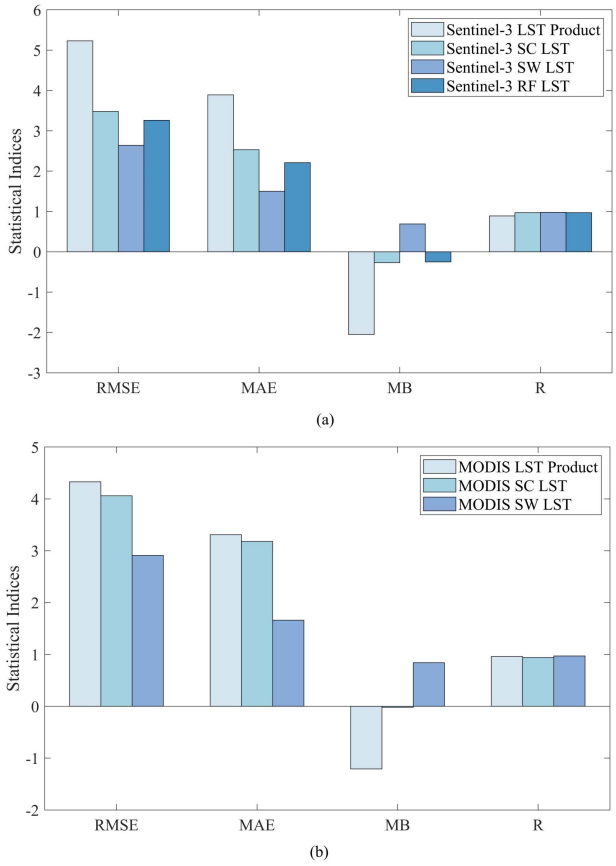

Fig. 7. Comparison of statistical metrics using different methods to retrieve LST based on sentinel-3 SLSTR (a) and MODIS data (b) against in situ measurements at six stations.

2.64 K to 3.48 K, Fig. 4) but a better performance than that of the MODIS LST products (MOD11A1) (see Fig. 7). Therefore, it is further proven that the improved SC and SW algorithms in this study can be used to accurately retrieve LSTs based on various satellite sensors.

B. Spatiotemporal Distribution of LSTs Over the TP

The SWA can provide more accurate LST over the TP by comparing different algorithms. To further assess the LST obtained by the SW algorithm, temporal variations in the SWA-based LST were compared with in situ measurements in the six study areas. The time series of SWA-based LST has good temporal consistency with the in situ LST at different meteorological stations (see Fig. 8). In particular, the SWA-based LST can capture some low values, such as those on 201(Doy), 2020, at BJ station [see Fig. 8(b)]. The annual LST at six stations ranged from 240 to 300 K, showing intense changes throughout the year.

The spatial distribution of the average SLSTR SWA LST results is shown in Fig. 9(a)–(h), and the MOD11A1 LST products at the same time are also provided for comparison [see Fig. 9(i)–(p)]. The spatial distribution of the SWA-based LST was generally consistent with that of MOD11A1. Compared with other regions in the TP, relatively high LST values can be identified in the Qaidam Basin (see Fig. 10). The Qaidam Basin is a huge closed intermountain basin and one of the four major basins in China, which is located between 90°16'E−99°16'E and 35°00'N-39°20'N. Previous study has proven that the Qaidam Basin has significant warming trends [46]. Furthermore, to quantitatively analyze the SWA LST and MOD11A1 LST, their minimum, maximum, and mean values were calculated over the TP (see Table VI). The results indicated that the mean value of MODIS LST is higher than that of SLSTR SWA-based LST during the daytime. The difference is mainly caused by the observation time and sensor characteristics of the two satellites. The daily LST variations are intense over the TP. The average satellite overpass time of SLSTR is approximately one hour earlier than that of MODIS, which may lead to differences in the spatial distribution of LST. Furthermore, the Sentinel-3 SLSTR S7-S9 bands start to saturate above 305 K and they are saturated at approximately 318 K, which leads to invalid values in extremely hot regions [32].

V. Discussion

Three different methods were developed to retrieve the LST over the TP based on Sentinel-3 SLSTR data. The generalized SC and SW algorithms were improved to retrieve LST with reasonable accuracy. In addition, four ML models were also used, and the performance of retrieving LST was limited by the number of input datasets. The results showed that the LST obtained by the improved SW algorithm was more reliable and accurate.

One of the most critical problems of LST retrieval based on satellite data is the accuracy and representativeness of validation at a satellite pixel scale. Generally, the LST varies enormously spatially and temporally, and it may be more than 10 K at a satellite pixel scale with some underlying surfaces [45]. The main limitation of ground-based validation is caused by spatial heterogeneity, which results in this validation method only being used for several relatively homogeneous land surface types. The error resulting from spatial heterogeneity can be reduced to a certain extent by establishing multiple stations at a satellite pixel scale and directly comparing the average measured LST with the satellite LST retrieval. It is worth noting that the land cover types of the six stations used in this study within 1 km are mainly bare soil and grassland (see Table II) [17]. The relatively unitary land cover types show that the land cover of the field stations is homogeneous to some extent. In addition, the spatial representativeness of the observations was assessed in this study, and the results show that all six stations meet the requirements of thermal homogeneity validation. Ma et al. [47] proposed a temporal variation method and defined a spatial representativeness indicator to evaluate a ground site's spatial representativeness. The validation results show that the effect of spatial representativeness on the ground stations is large, with MBs between −1.95 and 5.60 K. This method will also benefit the scientific community in the study of spatial representativeness.

The uncertainties of the retrieved LST may also come from the algorithm itself and sensor characteristics [18]. LST retrieval algorithms rely on different assumptions and simplifications of

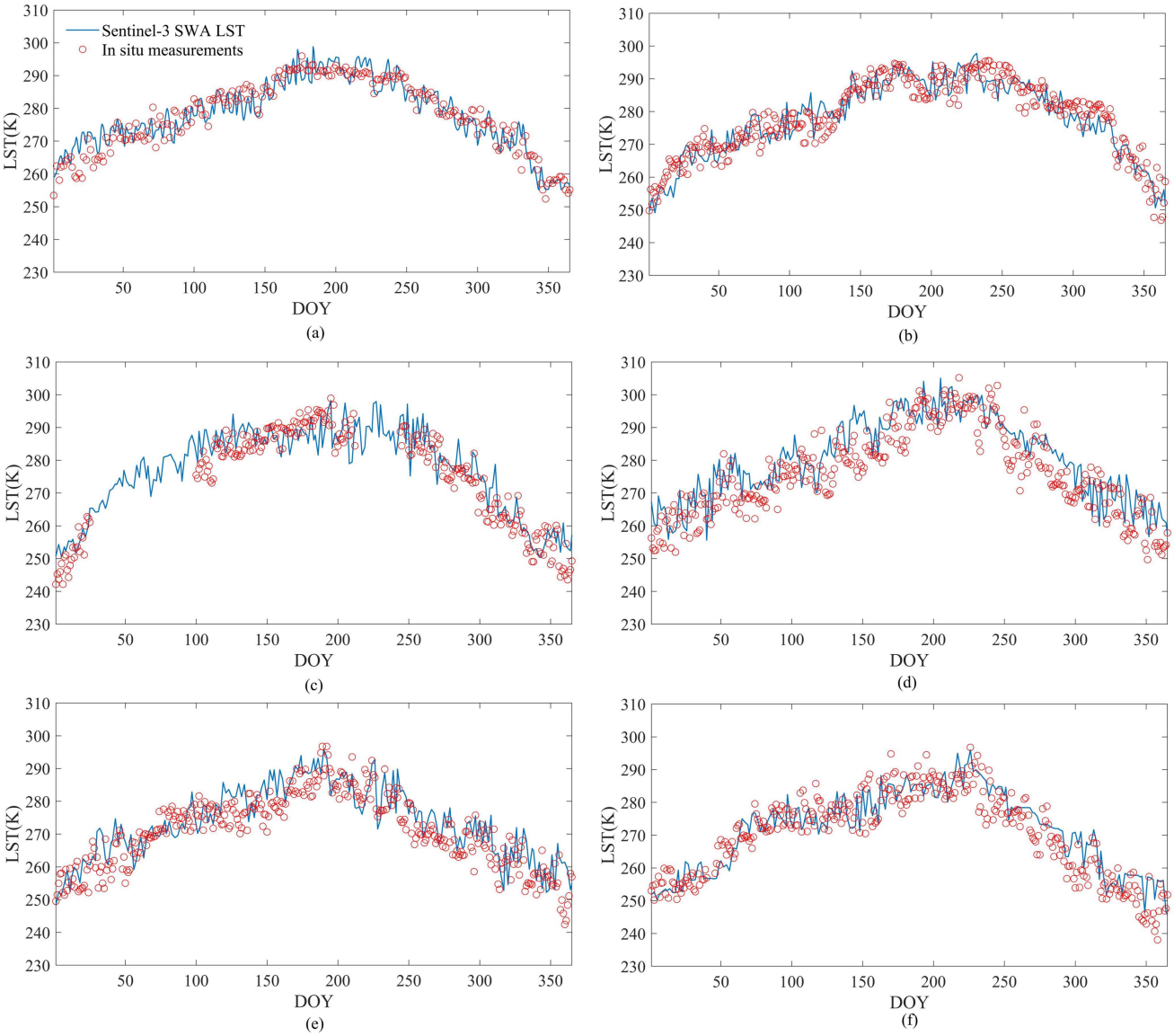

Fig. 8. Temporal variations in SWA LST and in situ LST data at SETORS (a), BJ (b), QOMS (c), NADORS (d), MAWORS (e), and NAMORS (f). The discontinuity of the open circles is primarily caused by the absence of in situ measurements.

the RTE to process the problem of ill-posed retrieval. These solutions might be inaccurate under certain circumstances. All LST retrieval algorithms used in this article provided that the LSEs are known a priori, and correct determination of LSE is the basis for LST retrieval. The algorithm of the official SLSTR LST products implicitly assumes and processes LSE knowledge [19]. In contrast, LSE was explicitly used in the SC and SW algorithms, which were calculated based on the statistical relationship between optical and near-infrared spectral information and LSE. The LSE quantitative retrieval process can be improved by using the advanced typical surface feature spectrum library. Additionally, TIR angular effects are especially obvious for polar-orbit satellites. The difference in LST observations between the nadir and off-nadir can reach 10 K for complex underlying surfaces [48]. Unfortunately, angular effects in LST retrieval from polar-orbit satellites are inevitable. In this study, the TIR angular effects were reduced by removing the areas with SZA greater than 40° and introducing the cosine of the SZA in the SW algorithm [49]. Geostationary satellites can make high-frequency measurements at fixed SZA, such as the Fengyun geostationary satellite, but their spatial resolutions are coarse. Hence, progress can be expected in developing new approaches for providing angularly normalized and time-continuous LSTs by combining multispectral and multitemporal TIR data [50].

The LST retrieved by TIR is mainly affected by WVC attenuation and LSE. Previous studies have indicated that when the WVC is greater than 3 g·cm^{-2}, the error in LST retrieval will become larger [17]. Specifically, for a hot and humid atmosphere, the error of LST retrieval increases by approximately 0.2 K when the WVC increases by 0.1 g·cm^{-2} [17], [51]. The WVC over the TP is lower than that of the surrounding regions, the mean WVC of the whole year ranges from 1.10 to 1.25 g·cm^{-2}. However,

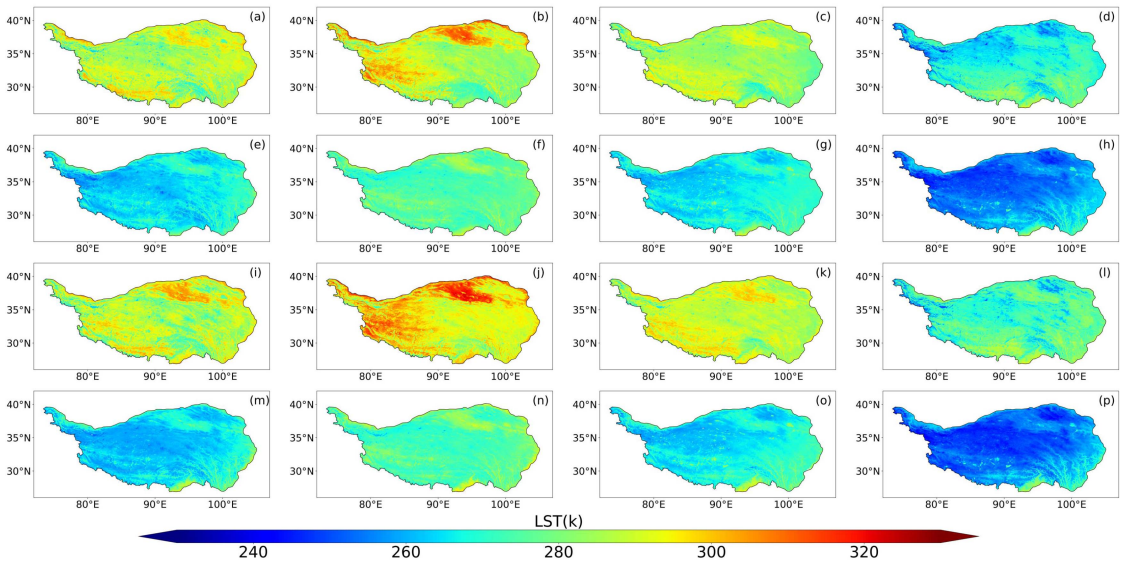

Fig. 9. Spatial distribution of the seasonal average LST from the SLSTR LST estimations and MODIS LST products (both at a 1 km × 1 km spatial resolution) in 2020 over the TP (unit: K). The rows show Sentinel-3 SLSTR (a)–(d) SWA daytime LST, (e)–(h) SWA nighttime LST, (i)–(l) MODIS daytime LST, and (m)–(p) MODIS nighttime LST. The columns (from left to right panels) show the spatial distributions in spring, summer, autumn, and winter.

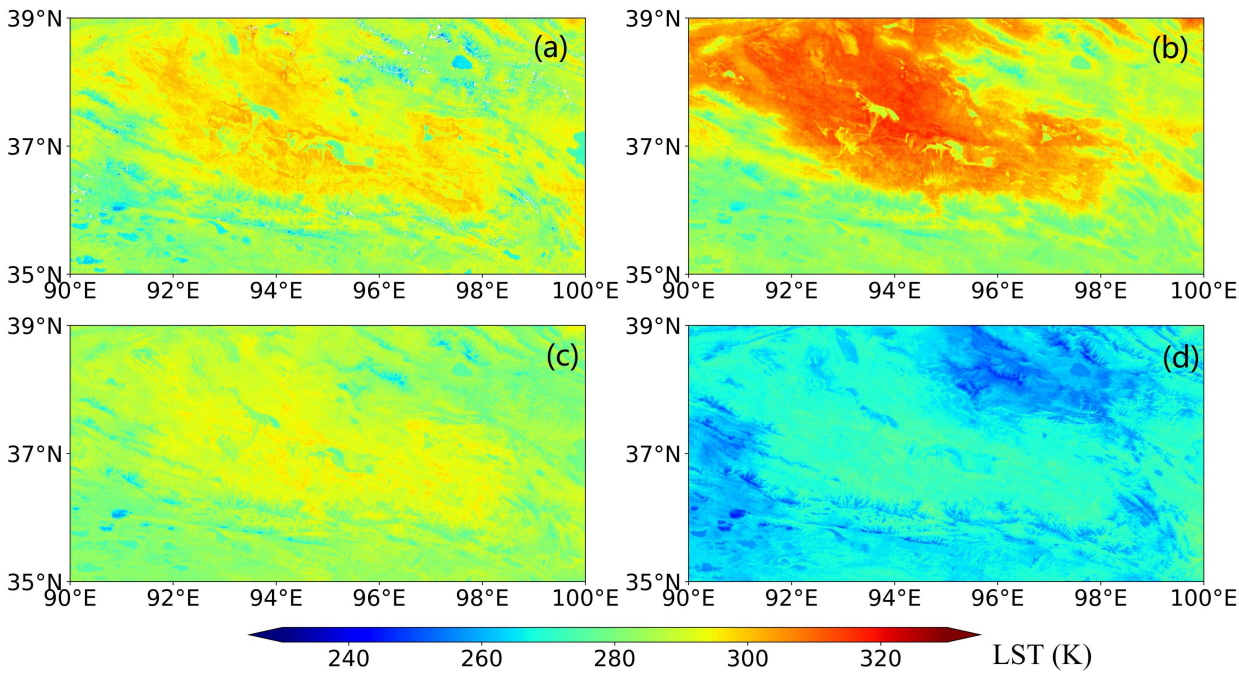

Fig. 10. Spatial distribution of the seasonal daytime LST from the SLSTR LST in 2020 over the Qaidam Basin (units: K). (a)–(d) represent the spatial distributions in spring, summer, autumn, and winter.

the WVC has high spatiotemporal variation characteristics over the TP. It is significantly higher in summer, about 2.11 g·cm^{-2}, accounting for more than 45% of the whole year [52]. Therefore, the WVC of the TP exerts strong influences on the accuracy of the LST retrieval. Furthermore, the uncertainty in LSE may lead to an error of 1 K to 2 K in LST when the LSE for most land surfaces can be known within a few percent [18], [53]. Because the spectral average emissivity of bare soil varies greatly with wavelength. The uncertainty of LSE retrieval is particularly obvious for the underlying surface of bare soil. However, most surfaces over the TP are heterogeneous and complex at satellite scale, and with up to 21 types of land cover [9]. In particular, bare soil is the largest land cover type, which occupy 54.8% of the TP's territory [17]. Compared with other regions, the uncertainty of LSE retrieval may cause larger error in LST. In addition, if the directionality of LSE is considered the LST retrieval errors will

TABLE VI
COMPARISONS OF STATISTICAL METRICS ASSOCIATED WITH SENTINEL-3 SWA LST AND MODIS LST PRODUCTS OVER THE TP IN 2020

Season	Day or Night	Sentinel-3 SLSTR			MODIS		
		Min (K)	Max (K)	Mean (K)	Min (K)	Max (K)	Mean (K)
Spring	Day	249.15	318.79	287.48	256.31	311.85	287.46
	Night	248.29	291.24	265.79	250.12	296.01	264.74
Summer	Day	262.93	319.52	289.77	262.72	324.99	296.56
	Night	258.24	298.33	275.79	251.64	299.92	275.42
Autumn	Day	252.86	306.96	284.05	251.38	307.08	288.43
	Night	248.25	294.60	266.86	240.46	295.16	266.90
Winter	Day	238.07	298.47	267.98	240.96	298.89	272.82
	Night	236.67	288.70	256.02	235.02	288.19	254.52

be larger. All the abovementioned factors will affect the LST retrieval accuracy over the TP [30].

There are two main problems in the application of ML models in satellite LST retrieval: the lack of physical interpretation and the limited input data. For the former, the combination of physical simulations and ML models may improve the physical understanding of LST retrieval [23]. Due to the limited amount of input data, the accuracy of the four ML models is obviously affected in this study. This limitation may be attributed to the missing SLSTR data and sparse distribution of ground stations in the TP, which may cause insufficient stability of the model and difficulty in dealing with different situations. To overcome these issues as much as possible, all available SLSTR data and ground stations with different underlying surfaces were selected. The selected stations with different land cover types (see Table II) include the main surface types over the TP, which can represent most areas of the TP to increase the stability of the model.

VI. CONCLUSION

High-accuracy LST over the TP based on satellite data is difficult to obtain because of some specific problems, such as limited measuring instruments, cloud contamination, and atmospheric effects. In this study, the improved SC and SW algorithms and four ML models are used to retrieve high-quality LST data over the TP based on Sentinel-3 SLSTR data. The results showed that the retrieval accuracy from our developed algorithms is better than that of the SLSTR LST products, and the SW algorithm with an RMSE of 2.64 K is much more accurate than the other methods. For ML models, sample data available for training are quite limited, resulting in a lower accuracy compared with the SW algorithm. The major conclusions can be drawn as follows.

1) The SC algorithm was utilized to retrieve LST based on Landsat images around six research stations to assess the spatial representativeness of in situ measurements. The error between 30 m and 1 km satellite pixels in the six study areas indicates that the validation stations used in this study are qualified for homogeneity validation.
2) Three different methods were improved to retrieve the LST based on SLSTR data on the TP. For the SC algorithms, the AFs suitable for CLDAS data were developed by the LR model, and the RMSE of the SC-based LST is 3.48 K. The validation results also show that the SW algorithm has satisfactory performance, and its RMSE is 2.64 K. Due to the limited number of training datasets, the accuracy of the four ML models is lower than that of the SW algorithm, and the RF model has the best accuracy with an RMSE of 3.26 K among the four ML models. The accuracy of the developed methods in this study is higher than that of the SLSTR LST products (5.23 K).
3) The time series of the SWA LST showed high temporal consistency with the in situ LST observed at different meteorological stations, and some abrupt changes in LST can also be captured. The SWA-based LST and MODIS LST products showed consistent spatial distributions, and relatively high LST value center can be identified in the Qaidam Basin.

REFERENCES

[1] Y. Y. Hu et al., "Estimation of the land surface temperature over the Tibetan Plateau by using Chinese FY-2C geostationary satellite data," *Sensors*, vol. 18, no. 2, Feb. 2018, Art. no. 376, doi: 10.3390/s18020376.
[2] N. Ge et al., "Estimations of land surface characteristic parameters and turbulent heat fluxes over the Tibetan Plateau based on FY-4A/AGRI data," *Adv. Atmos. Sci.*, vol. 38, no. 8, pp. 1299–1314, Aug. 2021, doi: 10.1007/s00376-020-0169-5.
[3] X. D. Zhang, J. Zhou, S. L. Liang, and D. D. Wang, "A practical reanalysis data and thermal infrared remote sensing data merging (RTM) method for reconstruction of a 1-km all-weather land surface temperature," *Remote Sens. Environ.*, vol. 260, Jul. 2021, Art. no. 112437, doi: 10.1016/j.rse.2021.112437.
[4] M. J. Zou, L. Zhong, Y. M. Ma, Y. Y. Hu, and L. Feng, "Estimation of actual evapotranspiration in the Nagqu river basin of the Tibetan Plateau," *Theor. Appl. Climatol.*, vol. 132, no. 3/4, pp. 1039–1047, May 2018, doi: 10.1007/s00704-017-2154-1.
[5] A. A. Mohamed, J. Odindi, and O. Mutanga, "Land surface temperature and emissivity estimation for urban heat island assessment using medium- and low-resolution space-borne sensors: A review," *Geocarto Int.*, vol. 32, no. 4, pp. 455–470, 2017, doi: 10.1080/10106049.2016.1155657.

[6] L. F. Zhang, W. Z. Jiao, H. M. Zhang, C. P. Huang, and Q. X. Tong, "Studying drought phenomena in the continental United States in 2011 and 2012 using various drought indices," *Remote Sens. Environ.*, vol. 190, pp. 96–106, Mar. 2017, doi: 10.1016/j.rse.2016.12.010.

[7] L. Zhong, Y. M. Ma, M. S. Salama, and Z. B. Su, "Assessment of vegetation dynamics and their response to variations in precipitation and temperature in the Tibetan Plateau," *Climatic Change*, vol. 103, no. 3/4, pp. 519–535, Dec. 2010, doi: 10.1007/s10584-009-9787-8.

[8] X. D. Liu and B. D. Chen, "Climatic warming in the Tibetan Plateau during recent decades," *Int. J. Climatol*, vol. 20, no. 14, pp. 1729–1742, Nov. 2000, doi: 10.1002/1097-0088(20001130)20:14<1729::Aid-joc556>3.0.Co;2-y.

[9] L. Zhong, Y. M. Ma, Y. K. Xue, and S. L. Piao, "Climate change trends and impacts on vegetation greening over the Tibetan Plateau," *J. Geophys. Res.-Atmos.*, vol. 124, no. 14, pp. 7540–7552, Jul. 2019, doi: 10.1029/2019jd030481.

[10] Y. M. Ma et al., "A long-term (2005-2016) dataset of hourly integrated land-atmosphere interaction observations on the Tibetan Plateau," *Earth Syst. Sci Data*, vol. 12, no. 4, pp. 2937–2957, Nov. 2020, doi: 10.5194/essd-12-2937-2020.

[11] D. L. Luo, H. J. Jin, S. S. Marchenko, and V. E. Romanovsky, "Difference between near-surface air, land surface and ground surface temperatures and their influences on the frozen ground on the Qinghai-Tibet plateau," *Geoderma*, vol. 312, pp. 74–85, Feb. 2018, doi: 10.1016/j.geoderma.2017.09.037.

[12] N. Pepin, H. J. Deng, H. B. Zhang, F. Zhang, S. C. Kang, and T. D. Yao, "An examination of temperature trends at high elevations across the Tibetan Plateau: The use of MODIS LST to understand patterns of elevation-dependent warming," *J. Geophys. Res.-Atmos.*, vol. 124, no. 11, pp. 5738–5756, Jun. 2019, doi: 10.1029/2018jd029798.

[13] F. Becker and Z. L. Li, "Surface temperature and emissivity at various scales: Definition, measurement, and related problems," *Remote Sens. Rev.*, vol. 12, pp. 225–253, 1995.

[14] J. Sheffield et al., "Satellite remote sensing for water resources management: Potential for supporting sustainable development in data-poor regions," *Water Resour. Res.,* vol. 54, no. 12, pp. 9724–9758, Dec. 2018, doi: 10.1029/2017wr022437.

[15] C. X. Shi, Z. H. Xie, H. Qian, M. L. Liang, and X. C. Yang, "China land soil moisture EnKF data assimilation based on satellite remote sensing data," *Sci. China Earth Sci.,* vol. 54, no. 9, pp. 1430–1440, Sep. 2011, doi: 10.1007/s11430-010-4160-3.

[16] P. C. Guillevic et al., "Land surface temperature product validation using NOAA's surface climate observation networks-scaling methodology for the visible infrared imager radiometer suite (VIIRS)," *Remote Sens. Environ.*, vol. 124, pp. 282–298, Sep. 2012, doi: 10.1016/j.rse.2012.05.004.

[17] X. Wang, L. Zhong, and Y. M. Ma, "Estimation of 30 m land surface temperatures over the entire Tibetan Plateau based on landsat-7 ETM+ data and machine learning methods," *Int. J. Digit Earth,* vol. 15, no. 1, pp. 1038–1055, Dec. 2022, doi: 10.1080/17538947.2022.2088873.

[18] Z. L. Li et al., "Satellite-derived land surface temperature: Current status and perspectives," *Remote Sens. Environ.*, vol. 131, pp. 14–37, Apr. 2013, doi: 10.1016/j.rse.2012.12.008.

[19] J. J. Yang, J. Zhou, F. M. Göttsche, Z. Y. Long, J. Ma, and R. Luo, "Investigation and validation of algorithms for estimating land surface temperature from sentinel-3 SLSTR data," *Int. J. Appl. Earth Obs.*, vol. 91, Sep. 2020, Art. no. 26548, doi: 10.1016/j.jag.2020.102136.

[20] Y. T. Zheng et al., "Land surface temperature retrieval from Sentinel-3A sea and land surface temperature radiometer, using a split-window algorithm," *Remote Sens.*, vol. 11, no. 6, Mar. 2019, Art. no. 23805, doi: 10.3390/rs11060650.

[21] J. Cristóbal, J. C. Jiménez-Muñoz, A. Prakash, C. Mattar, D. Skoković, and J. A. Sobrino, "An improved single-channel method to retrieve land surface temperature from the landsat-8 thermal band," *Remote Sens.*, vol. 10, no. 3, Mar. 2018, Art. no. 365214, doi: 10.3390/rs10030431.

[22] Z. M. Wan and J. Dozier, "A generalized split-window algorithm for retrieving land-surface temperature from space," *IEEE Trans. Geosci. Remote Sens.*, vol. 34, no. 4, pp. 892–905, Jul. 1996.

[23] H. Wang et al., "A method for land surface temperature retrieval based on model-data-knowledge-driven and deep learning," *Remote Sens. Environ.*, vol. 265, Nov. 2021, Art. no. 112665, doi: 10.1016/j.rse.2021.112665.

[24] Q. Q. Yuan et al., "Deep learning in environmental remote sensing: Achievements and challenges," *Remote Sens. Environ.*, vol. 241, May 2020, Art. no. 111716, doi: 10.1016/j.rse.2020.111716.

[25] Z. X. Yin et al., "Spatiotemporal fusion of land surface temperature based on a convolutional neural network," *IEEE Trans. Geosci. Remote Sens.,* vol. 59, no. 2, pp. 1808–1822, Feb. 2021, doi: 10.1109/tgrs.2020.2999943.

[26] K. B. Mao, J. C. Shi, Z. L. Li, and H. J. Tang, "An RM-NN algorithm for retrieving land surface temperature and emissivity from EOS/MODIS data," *J. Geophys Res.-Atmos.*, vol. 112, no. D21, Nov. 2007, Art. no. D21102, doi: 10.1029/2007jd008428.

[27] J. Yang et al., "The role of satellite remote sensing in climate change studies," *Nature Climate Change*, vol. 4, no. 1, pp. 74–74, Jan. 2014, doi: 10.1007/s11356-021-18005-0.

[28] D. J. Ghent, G. K. Corlett, F. M. Goettsche, and J. J. Remedios, "Global land surface temperature from the along-track scanning radiometers," *J. Geophys. Res.-Atmos.,* vol. 122, no. 22, pp. 12167–12193, Nov. 2017, doi: 10.1002/2017jd027161.

[29] C. Donlon et al., "The global monitoring for environment and security (GMES) sentinel-3 mission," *Remote Sens. Environ.,* vol. 120, pp. 37–57, May 2012, doi: 10.1016/j.rse.2011.07.024.

[30] K. Yang, H. Wu, J. Qin, C. G. Lin, W. J. Tang, and Y. Y. Chen, "Recent climate changes over the Tibetan Plateau and their impacts on energy and water cycle: A review," *Glob. Planet. Change*, vol. 112, pp. 79–91, Jan. 2014, doi: 10.1016/j.gloplacha.2013.12.001.

[31] H. R. Jiang et al., "Progress and challenges in studying regional permafrost in the Tibetan Plateau using satellite remote sensing and models," *Front Earth Sci.*, vol. 8, Dec. 2020, Art. no. 11501, doi: 10.3389/feart.2020.560403.

[32] P. Coppo et al., "SLSTR: A high accuracy dual scan temperature radiometer for sea and land surface monitoring from space," *J. Modern Opt.*, vol. 57, no. 18, pp. 1815–1830, 2010, doi: 10.1080/09500340.2010.503010.

[33] S. E. Hunt et al., "Comparison of the Sentinel-3A and B SLSTR tandem phase data using metrological principles," *Remote Sens.*, vol. 12, no. 18, pp. 2893–2893, Sep. 2020, doi: 10.3390/rs12182893.

[34] S. B. Duan et al., "Validation of collection 6 MODIS land surface temperature product using in situ measurements," *Remote Sens. Environ.*, vol. 225, pp. 16–29, May 2019, doi: 10.1016/j.rse.2019.02.020.

[35] H. Li et al., "Temperature-Based and radiance-based validation of the collection 6 MYD11 and MYD21 land surface temperature products over barren surfaces in Northwestern China," *IEEE Trans. Geosci. Remote Sens.*, vol. 59, no. 2, pp. 1794–1807, Feb. 2021, doi: 10.1109/tgrs.2020.2998945.

[36] E. Valor and V. Caselles, "Mapping land surface emissivity from NDVI application to European, African, and South American areas," *Remote Sens. Environ.*, vol. 57, no. 3, pp. 167–184, Sep. 1996, doi: 10.1016/0034-4257(96)00039-9.

[37] J. A. Sobrino and N. Raissouni, "Toward remote sensing methods for land cover dynamic monitoring: Application to Morocco," *Int. J. Remote Sens.,* vol. 21, no. 2, pp. 353–366, Jan. 2000, doi: 10.1080/014311600210876.

[38] Y. M. Ma et al., "Remote sensing parameterization of land surface heat fluxes over arid and semi-arid areas," *Adv. Atmos. Sci.*, vol. 20, no. 4, pp. 530–539, Jul. 2003, doi: 10.1007/BF02915496.

[39] J. A. Sobrino et al., "Land surface emissivity retrieval from different VNIR and TIR sensors," *IEEE Trans. Geosci. Remote Sens.*, vol. 46, no. 2, pp. 316–327, Feb. 2008, doi: 10.1109/tgrs.2007.904834.

[40] Z. Wan, Y. Zhang, Q. Zhang, and Z. L. Li, "Quality assessment and validation of the MODIS global land surface temperature," *Int. J. Remote Sens.*, vol. 25, no. 1, pp. 261–274, Jan. 2004, doi: 10.1080/0143116031000116417.

[41] J. Cristobal, J. C. Jimenez-Munoz, J. A. Sobrino, M. Ninyerola, and X. Pons, "Improvements in land surface temperature retrieval from the landsat series thermal band using water vapor and air temperature," *J. Geophys. Res.-Atmos.*, vol. 114, Apr. 2009, Art. no. D08103, doi: 10.1029/2008jd010616.

[42] J. C. Jimenez-Munoz and J. A. Sobrino, "A generalized single-channel method for retrieving land surface temperature from remote sensing data," *J. Geophys. Res.-Atmos.,* vol. 108, no. D22, Nov. 2003, Art. no. 4688, doi: 10.1029/2003jd003480.

[43] I. Ali, F. Greifeneder, J. Stamenkovic, M. Neumann, and C. Notarnicola, "Review of machine learning approaches for biomass and soil moisture retrievals from remote sensing data," *Remote Sens.*, vol. 7, no. 12, pp. 16398–16421, Dec. 2015, doi: 10.3390/rs71215841.

[44] T. Kattenborn, J. Leitloff, F. Schiefer, and S. Hinz, "Review on convolutional neural networks (CNN) in vegetation remote sensing," *ISPRS J. Photogrammetry*, vol. 173, pp. 24–49, Mar. 2021, doi: 10.1016/j.isprsjprs.2020.12.010.

[45] D. Long et al., "Generation of MODIS-like land surface temperatures under all-weather conditions based on a data fusion approach," *Remote Sens. Environ.*, vol. 246, Sep. 2020, Art. no. 111863, doi: 10.1016/j.rse.2020.111863.

[46] Y. J. Wang and D. H. Qin, "Influence of climate change and human activity on water resources in arid region of Northwest China: An overview," *Adv. Climate Change Res.*, vol. 8, no. 4, pp. 268–278, Dec. 2017, doi: 10.1016/j.accre.2017.08.004.
[47] J. Ma et al., "Continuous evaluation of the spatial representativeness of land surface temperature validation sites," *Remote Sens. Environ.*, vol. 265, Nov. 2021, Art. no. 112669, doi: 10.1016/j.rse.2021.112669.
[48] J. P. Lagouarde et al., "Modelling daytime thermal infrared directional anisotropy over Toulouse city centre," *Remote Sens. Environ.,* vol. 114, no. 1, pp. 87–105, Jan. 2010, doi: 10.1016/j.rse.2009.08.012.
[49] J. P. Lagouarde et al., "The MISTIGRI thermal infrared project: Scientific objectives and mission specifications," *Int. J. Remote Sens.,* vol. 34, no. 9/10, pp. 3437–3466, May 2013, doi: 10.1080/01431161.2012.716921.
[50] P. H. Wu, H. F. Shen, L. P. Zhang, and F. M. Göttsche, "Integrated fusion of multi-scale polar-orbiting and geostationary satellite observations for the mapping of high spatial and temporal resolution land surface temperature," *Remote Sens. Environ.*, vol. 156, pp. 169–181, Jan. 2015, doi: 10.1016/j.rse.2014.09.013.
[51] J. C. Jimenez-Munoz and J. A. Sobrino, "A single-channel algorithm for land-surface temperature retrieval from ASTER data," *IEEE Geosci. Remote Sens.*, vol. 7, no. 1, pp. 176–179, Jan. 2010, doi: 10.1109/lgrs.2009.2029534.
[52] K. P. Xu, L. Zhong, Y. M. Ma, M. J. Zou, and Z. Y. Huang, "A study on the water vapor transport trend and water vapor source of the Tibetan Plateau," *Theor. Appl. Climatol.*, vol. 140, no. 3/4, pp. 1031–1042, May 2020, doi: 10.1007/s00704-020-03142-2.
[53] P. Dash, F. M. Gottsche, F. S. Olesen, and H. Fischer, "Land surface temperature and emissivity estimation from passive sensor data: Theory and practice-current trends," *Int. J. Remote Sens.*, vol. 23, no. 13, pp. 2563–2594, Jul. 2002, doi: 10.1080/01431160110115041.

Yuting Qi received the B.S. degree in surveying and mapping engineering from Anhui Agricultural University, Hefei, China, in 2021. She is currently working toward the M.S. degree in atmospheric science with the School of Earth and Space Sciences, University of Science and Technology of China, Hefei, China.

Her research interests include algorithms for retrieval of land surface temperature over the Tibetan Plateau and construction of all-sky land surface characteristics.

Lei Zhong received the B.S. degree in geographic science in 2001 and M.S. degree in remote sensing and geographic information systems from Anhui Normal University, Wuhu, China, in 2004 and the Ph.D. degree in natural geography from the Institute of Tibetan Plateau Research, Chinese Academy of Sciences, Beijing, China, in 2008.

He is currently a Professor with the School of Earth and Space Sciences, University of Science and Technology of China, Hefei, China. His research interests include energy and water cycle processes between land surface and atmosphere, mainly including but not limited to energy and water cycle, land-atmosphere interaction, hydrometorology, atmospheric boundary layer process, application of remote sensing, etc.

Yaoming Ma received the B.S. degree in meteorology from Lanzhou University, Lanzhou, China, in 1987, the M.S. degree in atmospheric physics from the Lanzhou Institute of Plateau Atmospheric Physics, Chinese Academy of Sciences, Lanzhou, China, in 1995, the Ph.D. degree in atmospheric physics from National Okayama University, Okayama, Japan, in 2001, and the Ph.D. degree in environmental science from Wageningen University, Wageningen, The Netherlands, in 2006.

He is currently a Researcher with the Institute of Tibetan Plateau Research, Chinese Academy of Sciences. His research interests include atmospheric boundary layer observation and application of satellite remote sensing.

Yunfei Fu received the B.S. degree in synoptic dynamics from the Meteorology Institute, PLA Air Force, Beijing, China, in 1983, the M.S. degree in atmospheric physics and atmospheric environment from the School of Earth and Space Sciences, University of Science and Technology of China, Hefei, China, in 1990, and the Ph.D. degree in synoptic dynamics from the Institute of Atmospheric Physics, Chinese Academy of Sciences, Beijing, China, in 1993.

He is currently a Professor with School of Earth and Space Sciences, University of Science and Technology of China. His research interests include physical parameter retrieval of aerosol, cloud, precipitation, etc.

Xian Wang received the B.S. degree in atmospheric science in 2018 from the School of Earth and Space Sciences, University of Science and Technology of China, Hefei, China, where he is currently working toward the Ph.D. degree in geophysics with the School of Earth and Space Sciences.

His research interests include land surface temperature and evapotranspiration estimation over the Tibetan Plateau.

Peizhen Li received the B.S. degree in atmospheric science from the Chengdu University of Information Technology, Chengdu, China, in 2019. He is currently working toward the Ph.D. degree in geophysics with the School of Earth and Space Sciences, University of Science and Technology of China, Hefei, China.

His research interests include estimation of all-sky shortwave radiation over the Tibetan Plateau.